Systematic variation of design aspects for a significant increase in thermal fracture resistance of alumina microthrusters

OPEN ACCESS
IOP Publishing
Journal of Micromechanics and Microengineering
J. Micromech. Microeng. **31** (2021) 085005 (11pp)
https://doi.org/10.1088/1361-6439/ac0ad5

Systematic variation of design aspects for a significant increase in thermal fracture resistance of alumina microthrusters

Erika Åkerfeldt[1,*], **Lena Klintberg**[2] **and Greger Thornell**[1]

[1] Ångström Space Technology Centre, Uppsala University, Uppsala, Sweden
[2] Department of Materials Science and Engineering, Uppsala University, Uppsala, Sweden

E-mail: erika.akerfeldt@angstrom.uu.se

Received 1 April 2021, revised 19 May 2021
Accepted for publication 10 June 2021
Published 29 June 2021

Abstract

Because of thermal stresses occurring upon rapid heating or cooling, microcomponents made from high-temperature co-fired ceramics (HTCC) often fail at temperatures far below what the materials can withstand *per se*. This work investigates how resistance to thermal fracture in HTCC microcomponents can be increased by improving the component design, aiming at increasing the thermal performance of a microthruster with integrated heaters. The effect of four design parameters: component and cavity geometries (circular or square), heater location (central or peripheral), and addition of embedded platinum layers, on thermal fracture resistance was investigated through a full factorial designed experiment. Components of different designs were manufactured, and their thermal fracture resistance tested by rapid heating until failure. Peripheral heater location and presence of embedded platinum layers were seen to improve resistance to thermal fracture, whereas the shape of the component and the cavity did not significantly affect thermal performance. The most favourable design was then used for a cold gas microthruster that was fabricated and evaluated with respect to thermal fracture resistance. The microthruster survived rapid heating up to 1460 °C and was operated as a cold gas thruster at temperatures up to 772 °C, which is more than twice the maximum temperatures previously reported for alumina microthrusters.

Supplementary material for this article is available online

Keywords: HTCC, microthruster, thermal fracture, alumina

(Some figures may appear in colour only in the online journal)

* Author to whom any correspondence should be addressed.

1. Introduction

Miniaturization of spacecraft, with the main drive to reduce mass for subsequent reduction of mission and launch costs [1], has gained increasing interest recently. Small spacecraft also require small propulsion systems to fit the mass requirements [2] and to provide small thrust forces for precise positioning and attitude control [3]. If a thruster either produces thrust in the micro- or milli-Newton range, or is intended for use on a microspacecraft (mass less than 100 kg), it qualifies as a microthruster [4].

Thrusters can be categorized depending on their source of energy, and are generally split into electrical and chemical ones. Sometimes included in the latter category, sometimes categorized on their own, are cold gas thrusters, in which force is generated by expelling pressurized gas through a nozzle. Cold gas thrusters are simple and reliable [5], and are considered one of the most mature technologies for small spacecraft [6]. The main disadvantage of cold gas thrusters is their low specific impulse [5], a performance measure that describes how effectively a thruster uses its propellant. However, the specific impulse of a cold gas thruster increases with the temperature of the expelled gas [5], hence high-temperature operation improves the performance of such thrusters.

The use of microcomponents in high-temperature applications challenges the field of microtechnology. Silicon, the standard material for microcomponents, experiences degraded mechanical stability at temperatures above 600 °C [7]. Hence, at higher temperatures other materials must be employed. Ceramics are a popular choice due to their generally high melting points. In addition, ceramics are often chemically inert, making them useful in environments harsh also in other respects.

The co-fired ceramics technology is now established in microfabrication and has, for example, been used for realization of temperature [8], flow [9], pressure [10] and gas [11] sensors. The technology is divided into low- and high-temperature co-fired ceramics (LTCC and HTCC, respectively), where components made using the latter tolerate the highest temperatures of the two. HTCC microcomponents withstanding temperatures of above 1000 °C have been seen [12, 13]. However, ceramics are prone to fracture from thermal stresses caused by thermal gradients and transients occurring upon rapid heating and cooling. Hence, when the origin of high temperatures is heat provided by a component itself, for example from integrated heaters, rather than high-temperature surroundings, the component usually fails at temperatures far below what the materials can withstand *per se*.

The fracture toughness of a material describes its ability to resist crack growth and subsequent failure from cracking. The two most common dielectric materials used for HTCC components are zirconia and alumina. Zirconia has almost twice the fracture toughness of alumina [7], and can hence withstand larger stresses, including thermal ones. However, the ionic conductivity of zirconia makes the material electrically conductive above 700 °C [9]. For operation at higher temperatures, therefore, conductors must be isolated, resulting in more complicated processing.

The design of HTCC components has previously been seen to affect thermal performance. One example is [14], in which the effects of component and integrated heater sizes on thermal fracture resistance in a centimetre-scale gas sensor for automotive applications were evaluated. In [15], the thermal fracture resistance of an HTCC/LTCC mesoscale combustor was improved by increasing the thickness of the orifice plate. Furthermore, in [16], the effects on thermal performance of catalytic chamber, component and heater sizes in HTCC microthrusters were investigated.

In the field of spacecraft propulsion, the HTCC technology has been used for realization of cold gas [17], monopropellant [16] and vaporizing liquid [18] microthrusters from both zirconia [17, 18] and alumina [16]. However, failure from thermal stresses was encountered in all of these works, and for the case of alumina microthrusters with integrated heaters, the maximum failure temperature reported in dry tests is only 679 °C [16].

In this study, the effects of careful component design on thermal fracture resistance in HTCC microcomponents in general are experimentally investigated. The effect of four design parameters on thermal fracture resistance in alumina HTCC components is explored in a designed experiment. Components of different designs are fabricated, and their thermal fracture resistance is evaluated by rapid heating until the occurrence of failure. To make the study as generic as possible, properties present in a large variety of microcomponents are studied. The applicability of the results from is then demonstrated by using the most favourable design with respect to thermal fracture resistance for an alumina microthruster. This thruster is fabricated and evaluated, both in dry tests and during operation as a cold gas thruster.

2. Materials and methods

2.1. Design of generic components

For the first part of this study, generic microcomponents were designed. These contain two features common in HTCC components: a cavity and a screen-printed heater element. Four properties of the microcomponents were varied. (a) The component and (b) the cavity geometries were altered between circular and square, since circular features provide more symmetry, and sharp corners are associated with high stress concentrations. (c) The heater design was altered to obtain either central or peripheral heater location, which affects the heat distribution in the component. (d) Platinum layers, that could either work as thermal conductors or induce residual compressive stresses from mismatches between material properties, were added inside the component.

The four different design properties investigated here can be combined in a total of 16 different ways (figure 1). To make most use of a limited amount of samples, design of experiment (DOE) was employed, resulting in an experiment with a two-level full factorial design [19]. In this experiment, components of all 16 design combinations were included, and all were replicated. In addition, to evaluate variation, one of the combinations was replicated four times more. The selection of

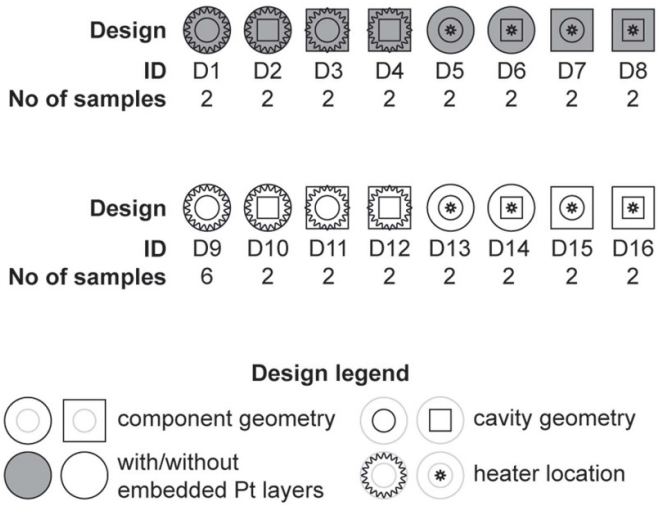

Figure 1. Component designs included in the two-level full factorial experiment, ID used for further referencing, and the number of components of each design included in the experiment.

this combination was arbitrary. In total, 36 components were included in the experiment.

The design of two of these components are seen in figure 2. Together they provide the dimensions of all individual properties, which can then be combined freely to give all 16 different possible component designs.

Each component consists of five alumina HTCC tape sheets. The three central sheets make up the cavity part. The top and bottom sheets contain the heaters and, if present, the embedded platinum layers. For components without embedded platinum layers, these layers are simply omitted. The incisions in the platinum layers are present to allow for a larger contact area between the adjacent ceramic sheets, to improve adhesion.

The two different heater patterns used to achieve heating at central and peripheral areas, respectively, were designed based on thermography images of similar heater designs presented in [20]. Component thickness was chosen within the range of 300–1100 μm found for HTCC microcomponents in literature [8–13, 16–18], many of which also contain cavities with single-sheet membranes [16, 17, 20, 21].

The design was completed with the intent to achieve as high thermal endurance as possible. Smaller components have previously been seen to endure higher temperatures than larger ones [9]. Hence, the component size was kept small. Furthermore, heaters were placed at both top and bottom sides of the component, since double-sided heating causes a more uniform temperature distribution. This will in turn result in a more uniform stress distribution across the component.

2.2. Fabrication of generic components

The components were fabricated using HTCC technology. The general fabrication scheme for co-fired ceramics is similar for both LTCC and HTCC. Ceramic sheets are individually structured through machining and screen printing of thick-film pastes. The sheets are then joined into 3D structures through

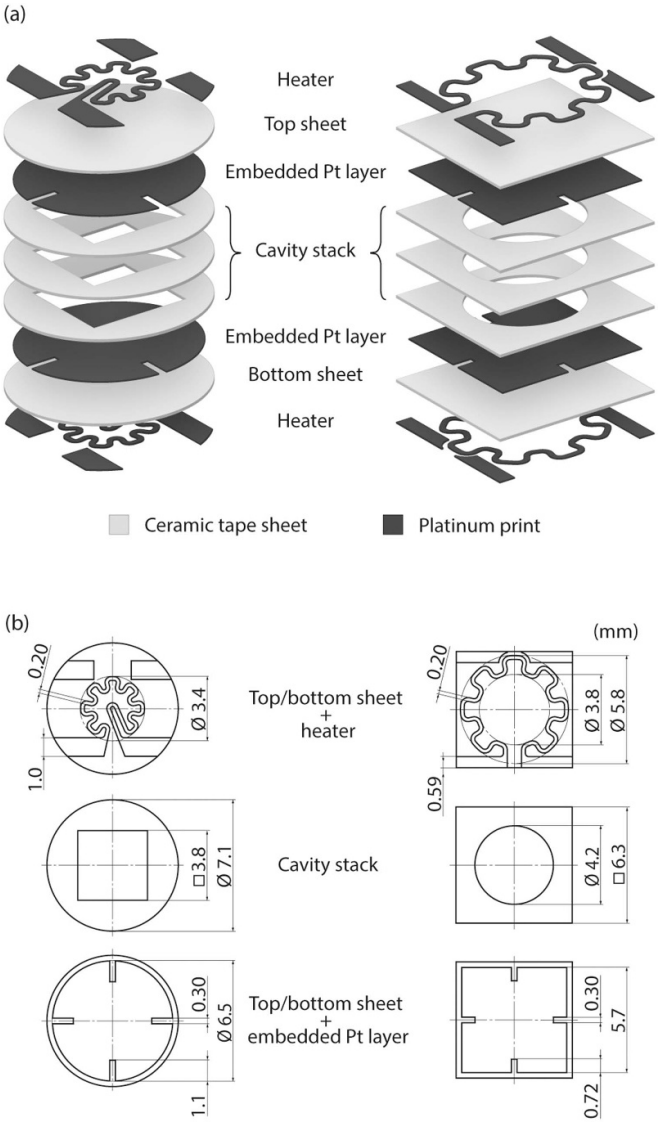

Figure 2. Exploded views of a component with circular component and square cavity geometries, embedded platinum layers and central heater location ((a); left), and a component with square component and circular cavity geometries, embedded platinum layers and peripheral heater location ((a); right), along with dimensions (b). All dimensions are prior to sintering.

lamination at elevated temperature and high pressure, with sacrificial material (e.g. graphite inserts) supporting any cavities. Finally, all constituents are fired at the same time, combusting the inserts and sintering the other materials. Overviews of the processing technology can be found in [22, 23].

Two component batches, each consisting of 36 components, were fabricated. All components with embedded platinum layers were contained in one batch, and all components without these layers were contained in the other.

The components were fabricated from 150 μm thick alumina green tapes (44007-150G, Ferro Corporation, OH, USA). For the cavity part, three tape sheets were pre-laminated at 70 °C and 3 MPa for 10 min [24]. Before lamination, the tape sheets were stacked between aluminium plates

(thickness 1 mm) and vacuum packaged using a food sealer (Chef Food Sealer, OBH Nordica, Denmark).

Cavities and alignment holes were then milled and drilled through all three sheets simultaneously using a printed circuit board plotter (ProtoMat S100, LPKF, Germany) and tools with diameters between 250 μm and 1 mm. To support the cavities during subsequent lamination steps, graphite inserts fitting snugly into the cavities were milled from a stack of four sheets of 125 μm thick graphite tape (49000-G, Ferro Corporation, OH, USA), that had been pre-laminated in the same fashion as the alumina green tapes.

The top and bottom sheets of the components without embedded platinum layers were prepared by screen printing the heater patterns using platinum paste (5571-G, *ibid*) in a manual stencil printer (ProtoPrint S, LPKF, Germany) with a stainless steel mesh screen (LaserTech Services, Denmark). For the components containing the embedded platinum layers, the top and bottom sheets were prepared by first screen printing the platinum layers using a mixture of leftover pastes (5571-G and 5574-A, Ferro Corporation, OH, USA, exact mixing ratio unknown). Then, alignment holes of diameter 1.1 mm were drilled using the plotter. Finally, the heater pattern was screen printed on the opposite side of the sheet using platinum paste (5571-G, *ibid*), utilizing the alignment holes for correct placement of the pattern.

The processed cavity part along with the top and bottom sheets were stacked in a fixture with alignment pins [16]. This five-sheet tape stack, along with the fixture, was vacuum packaged, and the tapes were joined together through a 10 min lamination at 70 °C and 3 MPa. The fixture was then replaced by the aluminium plates, and the stack was once again vacuum packaged before another 10 min lamination, this time at 70 °C and 21 MPa, took place.

After this final lamination, individual components were contoured using the plotter.

The conductive leads on the back side of the components were joined to connection pads at the top side by manually adding platinum paste (5571-G, *ibid*) over the edge, followed by drying at 50 °C for 1 h.

Finally, the samples were fired in a high-temperature furnace (ECF 20/18, Entech, Sweden), following a firing profile with a peak temperature of 1550 °C [21].

In a few components, the heater patterns or the over-the-edge platinum connections were found non-conductive after firing. Post-firing repair of broken heaters and over-the-edge platinum was done by manually applying silver paste (CN33-145 Ag, Ferro Corporation, OH, USA), followed by treatment in a muffle furnace (Thermolyne FB1310M, Thermo Scientific, MA, USA) at 820 °C for 17 min.

For evaluation of the sintering shrinkage mismatch between alumina tapes and platinum prints, two pieces of alumina tape, about 6 × 6 mm^2, were cut using a scalpel, and platinum prints of approximately the same size were screen printed on a sheet of graphite tape. The graphite tape served as a carrier, and was intended to combust during firing and leave free-standing prints behind. Three prints were made, two using the 5571-G paste, and one using the 5574-A paste. The alumina pieces and platinum printed graphite tapes were then fired following the same procedure as for the components. During firing, the samples were placed between two porous alumina plates (ZAL-45AA, 0.25″T, Zircar Ceramics, NY, USA) to maintain their flatness. The dimensions of the tapes and prints were measured prior to and after firing. Four dimensions were measured on each tape piece, and two on each print. All measurements were repeated three times.

2.3. Evaluation of generic components

All components were inspected using optical microscopy and x-ray (XT V 130, Nikon, Japan). The quality of the screen-printed heaters was further evaluated by two-point measurement of the heater resistances using a multimeter (34450A, Agilent, CA, USA).

The sintering shrinkage of the alumina pieces and platinum prints were evaluated by measuring their dimensions prior to and after sintering using a measuring microscope (MM40, Nikon, Japan) with digital readout (Quadra Chek 200, Metronics, NH, USA).

During the evaluation of thermal endurance, a custom-made stage was used (cf. figure 4). In this, components were supported by four pillars made from pieces of alumina tube (length 10 mm and outer diameter 1.5 mm; Degussit AL23, Kyocera Fineceramics Solutions, Germany). The tubes were attached to a 4 × 4 cm^2 sheet of printed circuit board (PCB) laminate (RO4003C, Rogers Corporation, AZ, USA) in which holes for the pillars were milled using the plotter. The pillars were further fastened to the PCB using a small amount of glue (Araldite Rapid, Huntsman Advanced Materials, TX, USA). During testing, the components rested on the pillars with contact points at the periphery of both the components and the pillars, to minimize the contact area between the component and the stage to reduce the thermal impact from the stage.

During the evaluation, the screen-printed heaters on the top and bottom sides of the component were connected in series to a power supply (QL355TP, TTi, UK). All electrical connections to the components were achieved using probe needles (72G-J3/120, American Probe and Technologies, CA, USA).

The temperature at the top surface of the component was monitored using an IR camera (Thermovision A30, FLIR Systems, Sweden) equipped with a macro lens (Macro-lens 18 micron, *ibid*). To determine the correct emissivity of the alumina used here, calibration of the IR image along with a Pt-100 element fastened to the top component surface was performed. The component was resistively heated using the screen-printed heaters during simultaneous observation of the component surface with the IR camera. The emissivity was adjusted until the maximum temperature obtained in the IR image matched the temperature given by the Pt-100 element. Calibration was performed at 11 different temperatures spanning between 22 °C and 916 °C.

Since the IR camera only measures temperatures between 50 °C and 1200 °C, the temperature of components exceeding 1200 °C was determined from the power supplied. In a plot of temperature versus power for results attained at temperatures less than 1200 °C, a linear fit was made to the nine last measurements attained below 1200 °C (see example in

supplementary figure S1 (available online at stacks.iop.org/JMM/31/085005/mmedia)). The linear fit was then extrapolated to higher powers and used for determination of temperatures above 1200 °C.

From all components fabricated, 36 components were selected for the full factorial experiment (figure 1). These had heaters with as low resistance as possible, and as equal resistance as possible among the top and bottom heaters, both factors indicating good heater quality.

The resistance to thermal fracture was evaluated by heating the components resistively using the screen-printed heaters until failure, while monitoring the surface temperature using the IR camera. The current supplied to the heaters was increased in steps, with cooling to room temperature prior to every increment. Hence, each current level corresponds to one heating cycle from room temperature to steady state, defined as when the maximum surface temperature attained in the IR image had settled. The approximate time for this was noted.

For the first components tested, currents starting at 300 mA for components with central heater location and 250 mA for components with peripheral heater location were used. This corresponded to a maximum surface temperature of about 300 °C. Later, the starting current was increased to 400 mA and 330 mA, respectively, corresponding to a maximum surface temperature of about 500 °C.

The current was gradually increased in steps of 10 mA, aiming for an increase in steady-state temperature of about 30 °C per step. This was continued until component failure.

The two-level full factorial experiment was analysed using a computer software (MODDE Pro 11, Umetrics, Sweden) to identify how the individual properties affect the failure temperature. In this analysis, the four design properties were treated as qualitative factors, each with two discrete levels. The experimentally obtained failure temperatures were used as the response variable. All data were centred and scaled. Partial least squares regression was then used to model the relationship between the design properties and the failure temperatures, and to determine the effect of each property. Analysis was performed by first fitting a full factorial model to the experimental data, and then reducing it by excluding non-significant factors, following the procedure described in [19].

2.4. Design of microthruster

After evaluation of the generic microcomponents, the most favourable design was used for a microthruster. According to the result from the first part, to increase resistance to thermal fracture, a peripheral heater location should be used, and platinum layers embedded. Component and cavity geometries were not seen to affect thermal performance, but the higher degree of symmetry as well as the lack of sharp corners otherwise accounting for stress concentrations in square components still make circular geometries a better choice.

To move from the generic microcomponents into a microthruster, two additional features needed to be implemented: a nozzle and a gas inlet hole along with the possibility of gas connection. It shall be noted that the design objective for the microthrusters was not to optimize thruster performance.

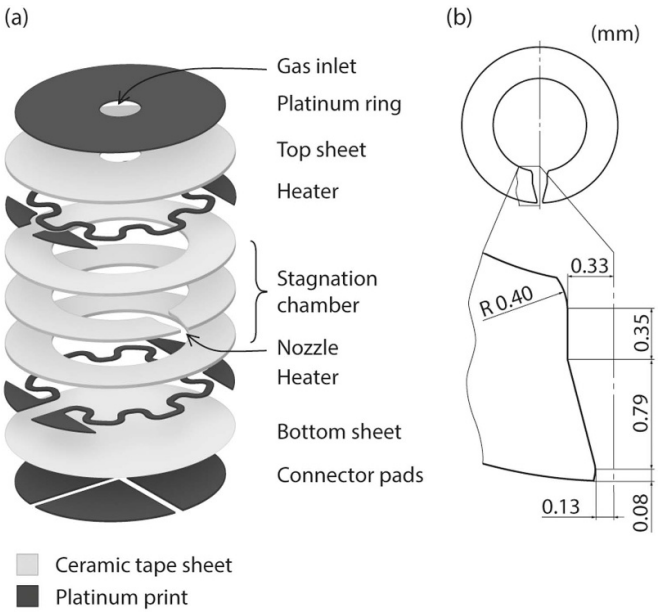

Figure 3. Exploded view of the microthruster (a) along with a selection of the dimensions of the nozzle (b). All dimensions are prior to sintering.

Instead, the purpose of the microthruster was to demonstrate the applicability of the results from the first part of this work.

The microthruster, figure 3, consists of five HTCC tape sheets. The three central ones form the stagnation chamber, with the nozzle contained in the middle sheet to maintain vertical symmetry. The top sheet contains the gas inlet hole surrounded by a platinum ring used for the gas connector, and a heater. The bottom sheet contains the other heater and electrical connector pads.

To maintain symmetry, the inlet hole was positioned at the centre of the top sheet. The hole is 1.3 mm in diameter, and surrounded by a screen printed platinum ring for the gas connection. Since the ring occupies the top surface, the heaters were placed on the inside of the top and bottom sheets. Due to the heaters being located at the inside of these sheets, the embedded platinum layers had to be excluded, even though they were previously seen to improve resistance to thermal fracture. The design of the nozzle was adapted from a thruster suitable for atmospheric ambient developed in [25], by increasing all dimensions with 25% to allow for the size reduction occurring during sintering. The dimensions not shown in figure 3 can be derived from [25] and the dimensions of the generic microcomponents in figure 2.

For practical reasons, the screen used for screen printing of the generic microcomponents was reused for the prints in the microthruster. Hence, the prints for the platinum ring and the connector pads were achieved using the screen pattern previously used for printing of the embedded platinum layers. The platinum ring was achieved by printing five such patterns on top of each other, each with a slight offset to the previous one to fill out the incisions in the pattern, and the connector pads were achieved by printing one such pattern followed by milling two orthogonal trenches in it to allow for four separate connectors.

2.5. Fabrication of microthrusters

One batch, consisting of 18 microthrusters, was fabricated using the same process and materials as for the generic microcomponents.

For the stagnation chamber part, the nozzle sheet was prepared by milling the nozzle and drilling alignment holes in an alumina green tape using the plotter. The nozzle sheet was then stacked between two other tape sheets, through which alignment holes had been drilled, in the alignment fixture. During stacking, milled graphite inserts were positioned inside the nozzles. The three tape sheets were then pre-laminated for 10 min at 70 °C and 3 MPa, before the stagnation chamber was milled through all three sheets simultaneously.

The top sheet was prepared by screen printing of the heater pattern using platinum paste (5571-G, Ferro Corporation, OH, USA), followed by a 10 min lamination at 70 °C and 21 MPa between aluminium plates. This lamination was performed to press the print into the tape sheet, to avoid damage to the print caused by the cavity edges during subsequent lamination steps. Alignment holes were then drilled before the platinum ring at the top was screen printed on the opposite side of the sheet using platinum paste (5574-A, *ibid*). Each of the five prints was followed by drying at 50 °C for about 1 h.

The bottom sheet was prepared by screen printing of the heater pattern, lamination and drilling of alignment holes in the same fashion as for the top sheet. The embedded platinum layer design was then screen printed on the opposite side of the sheet using platinum paste (5571-G, *ibid*), followed by milling two orthogonal trenches using the plotter to obtain four separated connector pads.

The processed stagnation chamber part along with the top and bottom sheets was then subjected to the two-step lamination procedure, with a first 10 min lamination at 70 °C and 3 MPa and a final one with the same duration at 70 °C and 21 MPa. After final lamination, gas inlet holes were milled through the top sheet and individual thrusters were contoured, all using the plotter.

The heater patterns were joined to the electrical connector pads at the bottom side by manually adding platinum paste over the edge. Two layers of platinum were applied, each followed by drying at 50 °C for 1 h.

Finally, the thrusters were fired in the high-temperature furnace, following the same procedure as for the generic components.

Some thrusters were prepared for gas connection by attaching 4 cm long parts of alumina tube (Degussit AL23, 3 × 1.6 mm, Kyocera Fineceramics Solutions, Germany) to the platinum ring surrounding the gas inlet hole using platinum paste (5571-G, Ferro Corporation, OH, USA). After this, a second firing procedure in the high-temperature furnace took place, this time with a peak of 2 h at 1400 °C. Polyurethane tubing (length 1 dm, outer/inner diameters 6/4 mm, respectively) was then glued to the end of the alumina tube using epoxy (Epo-Tek 730, Epoxy Technology, MA, USA) to allow for further gas connection.

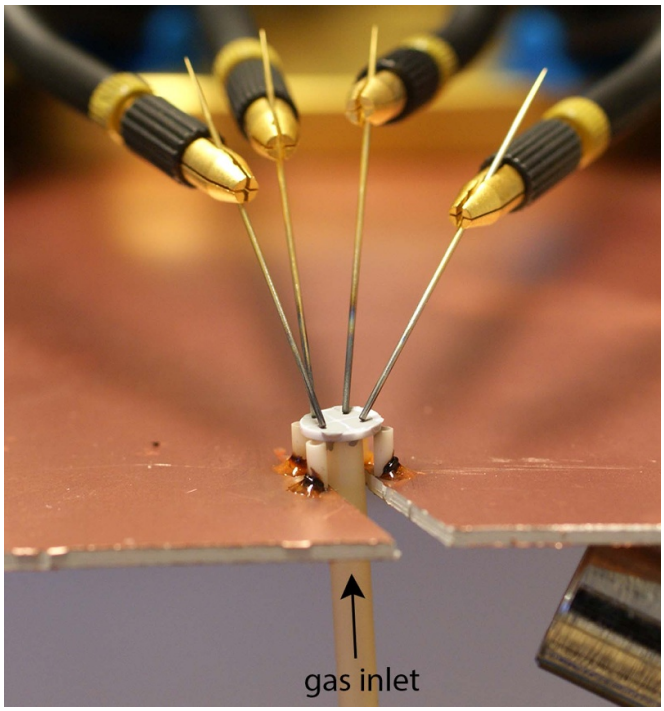

Figure 4. A thruster with alumina tube for gas connection attached, mounted in the test setup. The IR camera (not visible in this image) overlooks the component from above. The metal part at the bottom right corner acts as a mechanical support for the stage.

2.6. Evaluation of microthrusters

To evaluate the quality, all thrusters were inspected using optical microscopy. The quality of the screen-printed heaters was evaluated by two-point measurement of the heater resistances using a multimeter (Fluke 77 Multimeter, Fluke, WA, USA).

The thermal endurance of two stand-alone thrusters, without alumina tube attached, was evaluated using the same setup and procedure as for the generic microcomponents, with cycling from room temperature to a step-wise increased steady-state temperature. The only exception was that the current increment size was adjusted so that every increment still corresponded to an increase in steady-state temperature of about 30 °C. This was achieved using step sizes of 10–20 mA.

To evaluate the effect of attaching the alumina tube, the thermal endurance of one thruster with tube attached was also evaluated. To allow for the tube, another stage was fabricated, resembling the previously used one but with a cut-out in the PCB laminate through which the tube could pass. The thruster rested on the four pillars as previously, and the tube hung freely from the thruster, figure 4. For evaluation of thermal performance, the same test procedure as for the stand-alone thrusters was used.

Two thrusters were evaluated during operation as cold gas thrusters. For this evaluation, the modified fixture with cut-out was used, and the plastic tubing was further connected to a gas supply. The thrusters were fed with pressurized nitrogen gas

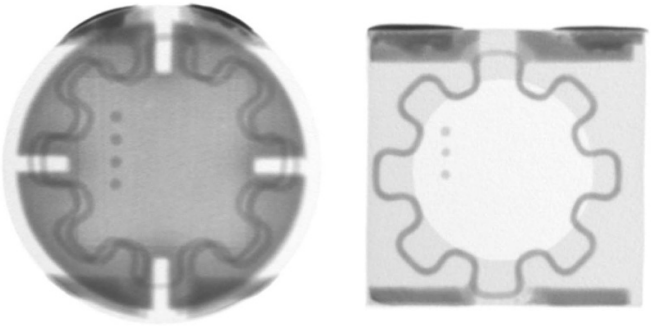

Figure 5. X-ray images of a D2 component with embedded platinum layers (left), and a D11 component without embedded platinum layers (right), both suffering from some misalignment. The small platinum dots are used for sample identification.

Table 1. Results from resistance measurement of heaters in the generic microcomponents. Average presented along with standard deviation.

Heater location	Total no. of heaters tested	No. of non-conductive heaters	Average functional heater resistance (Ω)
Central	72	1	4.6 ± 0.63
Peripheral	70	7	6.7 ± 1.3

with an overpressure of 200 kPa. With the gas flowing through the thrusters throughout the test procedure, thermal endurance was evaluated using the same test procedure as for the testing of thrusters with tube.

3. Results

3.1. Generic microcomponents

3.1.1. Inspection. After one component was lost to the exhaust system of the plotter, the fabrication resulted in a total of 71 generic microcomponents. Figure 5 shows x-ray images of two components, revealing the inside of the components as well as some misalignment between tape sheets, present to some degree in almost all components.

Resistance measurements of the heaters, table 1, showed that 94% of the heaters investigated were conductive. Optical microscopy and x-ray inspection of the non-conductive heaters revealed cracks in the heaters at positions located over the edges of the cavity. Of the eight dysfunctional heaters, seven were found in components from one batch, indicating quality differences not uncommon in this type of fabrication.

Broken heaters in four components (one each of D1, D11, and two of D9) and over-the-edge platinum in another one (of D1), all needed to fulfil the full factorial experiment, were repaired using silver paste (see section 2.2).

The shrinkage of the alumina tape and the platinum pastes is presented in table 2.

Table 2. Average shrinkage of the tape and pastes presented along with standard deviation. $N = 24$ for the alumina tape, 12 for the 5571-G paste and 6 for the 5574-A paste.

Material	Average shrinkage (%)
Alumina tape	15.0 ± 0.395
Platinum paste 5571-G	23.1 ± 2.43
Platinum paste 5574-A	31.0 ± 1.04

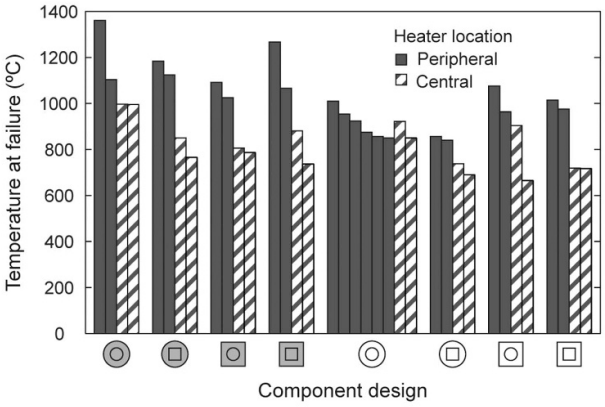

Figure 6. Maximum surface temperatures at failure for all components included in the full factorial experiment. Symbols denoting component design are explained in figure 1.

3.1.2. Thermal endurance. The emissivity calibration was performed using a D1 component, not included in the full factorial experiment, and resulted in three discrete emissivity values used in different temperature ranges.

Maximum surface temperatures obtained at failure are presented in figure 6.

For the D9 component used to evaluate variation, the average failure temperature was 917 °C ± 42 °C, using a 95% confidence interval.

Of the 36 components tested, 13 failed by cracking completely into two or more separate pieces, nine from cracks visible in optical microscopy, and three from melting of the heater. For the remaining 12 components, no visible cracks nor any melting of the heater were seen.

Two examples of IR images obtained at failure temperature are seen in figure 7. Qualitative evaluation of IR images obtained at failure temperature and at about 500 °C for all components was performed. From this, it was seen that a peripheral heater location gives a more uniform temperature distribution than a central one. Components with embedded platinum layers were not seen to have a more uniform temperature distribution than components without, but withstood larger temperature differences across the surface at failure. This was extra prominent in components with peripheral heater location.

The time required from turning on the current until steady state was reached was about 90 s, no matter the final temperature reached.

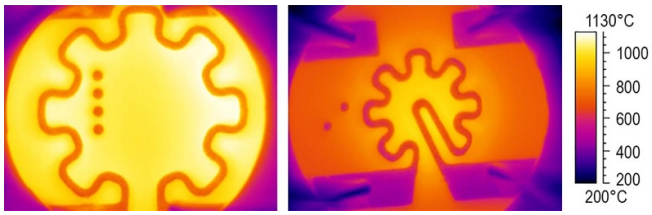

Figure 7. IR images obtained at failure temperature for components of design D1 (left) and D5 (right). Maximum surface temperatures in the images are 1124 °C and 997 °C, respectively. Since the IR images are calibrated for the emissivity of alumina, the temperatures of metal parts are not correct.

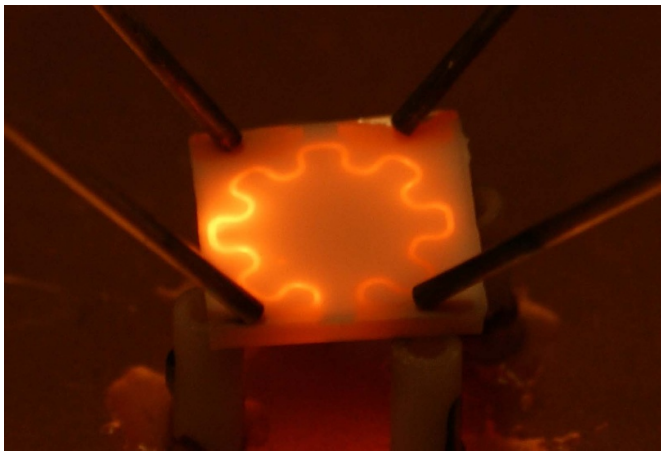

Figure 8. Hot spots caused by width variations in the heater pattern, seen during visual inspection of the glowing heater, where higher temperature of the heater results in a brighter glow.

Local variations in heater width were seen to cause local hot spots on the component surface. This could be seen both from IR images as well as by visual inspection of the sample during testing at temperatures above 700 °C, where platinum starts to glow, figure 8.

3.1.3. Data analysis. According to the reduced model resulting from the data analysis, the only factors that significantly affected failure temperature were heater location and embedded platinum layers. No other factors included in the full factorial experiment, including all interaction terms, significantly affect the failure temperature according to the model. The effects of all primary factors are presented in table 3.

Figure 9 shows experimentally observed failure temperatures versus failure temperatures predicted by the model. The goodness of fit, R^2, of the model is 0.64, and its goodness of prediction, Q^2, is 0.58.

3.2. Microthrusters

As for the generic microcomponents, one thruster was lost during fabrication. Hence, the fabrication resulted in a total of 17 microthrusters, two of which are seen in figure 10. Optical microscopy revealed that three thrusters had clogged nozzle outlets. (Being featureless, these images have been left out.)

Table 3. Design factors' effect on failure temperature according to the reduced model, along with 95% confidence interval.

Design change	Increase in failure temperature (°C)
Changing from central to peripheral heater location	226 ± 70
Embedding platinum layers	155 ± 70
Changing from square to circular cavity	Not significant
Changing from square to circular component	Not significant

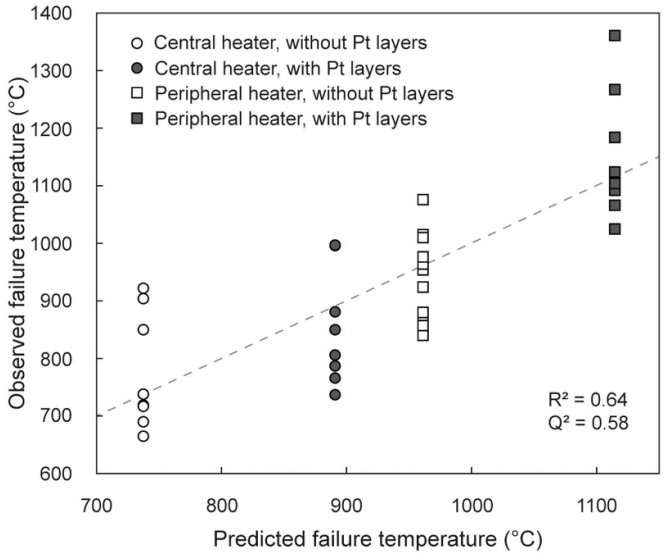

Figure 9. Experimentally observed failure temperatures versus failure temperatures predicted by the model. The dashed guide line indicates where the observed temperature equals the predicted one.

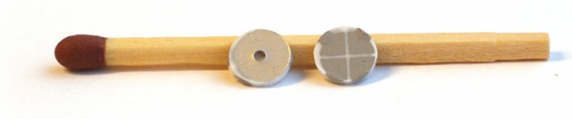

Figure 10. Two microthrusters leaning against a normal match. Left one shows top side containing gas inlet hole and right one shows the electrical connector pads on the bottom side.

No cracks in the platinum prints at locations over the edges of the cavity were seen.

Resistance measurements of the heaters revealed that all 34 heaters were conductive, with an average resistance and standard deviation of 6.9 Ω ± 0.56 Ω after exclusion of one outlier with a suspiciously high resistance of 10 Ω.

In testing of stand-alone thrusters, the first thruster tested reached 1460 °C, before the connection through the probe needles failed. The second thruster tested reached 1290 °C before testing was aborted to avoid further problems with the probe needles.

In dry testing of the thruster with an alumina tube attached, the thruster reached 1220 °C before testing was aborted. Heating the thruster from room temperature to steady state took about 2.5 min.

During operational testing, the two thrusters tested reached 417 °C and 772 °C, respectively, before the alumina tube detached. Heating the thrusters to steady state took about 3 min.

4. Discussion

According to the results from the first part of this work, peripheral heater location and embedded platinum layers were seen to increase resistance to thermal fracture. The increase provided by the peripheral heater location is a result of this location causing more uniform heating of the component compared to central location, which reduces the temperature gradients.

For the embedded platinum layers, two different effects were hypothesized: for the layers to serve as heat distributors, or to induce residual compressive stresses in the alumina. Since platinum has higher thermal conductivity (71 W m^{-1} K^{-1} at 0 °C [7]) than alumina (30–40 W m^{-1} K^{-1} at room temperature [26]), the layers could contribute to a more uniform heat distribution that could increase the resistance to thermal fracture. However, no evidence of more even temperature distributions in components with platinum layers was seen. Instead, it appeared that components with embedded platinum layers could withstand larger temperature differences across the surface before failure. This could imply that platinum provides a mechanical reinforcement, e.g. through inducing residual compressive stresses in the alumina during fabrication. The sintering mismatch and residual stresses formed upon co-firing of alumina and zirconia has been studied previously [27], but similar effects for the combination of alumina and platinum has not been investigated. The shrinkage measurements conducted here indicate that platinum shrinks more than alumina during firing. Hence, occurrence of residual compressive stresses in the alumina is likely. However, this study does not attempt to make a thorough characterization of the stress situation in a material system of HTCC alumina and platinum, and further study of this is needed before final conclusions can be drawn.

Regarding the shrinkage measurements, it should be noted that all platinum prints adhered to either the top or the bottom porous plate that supported the prints during firing. This caused uneven shrinkage and warping of the prints, which contributes to the relatively large standard deviation in the shrinkage of the prints compared to the shrinkage of the alumina tape. The mixing ratio of the paste that was used for printing of the platinum layers in the generic components was unknown. However, this is not thought to affect the effect of the printed layers since both pastes shrink more than the alumina tape upon firing. Hence, any mixture of these two pastes would have the intended effects.

In addition to effects from shrinkage, Young's modulus of platinum differs from that of alumina (171 GPa [7] and 380–410 GPa [26], respectively), and an interface between layers of different stiffness can affect crack propagation and increase material strength [28].

The goodness of fit of the model, R^2, representing how well the experimental values fit the predicted values, was 0.64, and the goodness of prediction, Q^2, describing the model's ability to predict failure temperatures, was 0.58. A model based on experimental data is considered good when $Q^2 > 0.5$ and the difference between Q^2 and R^2 is not exceeding 0.3 [29]. In addition to the variations caused by the experiment, the strength in ceramic materials always experiences some variations due to the mechanisms governing fracture in brittle materials. Hence, the reduced model is reasonable. Furthermore, the variation between replicates, evaluated for the D9 component, is much smaller than the overall variation in failure temperatures among all components. This indicates that the effects seen are not only because of random variations or experimental error. During the emissivity calibration, the Pt-100 element covered an area of about 2×2 mm^2 at the central part of the component, leaving only the outer part of the component visible in the IR camera. Hence, during calibration, the Pt-100 element measured the average temperature of the central part of the component, which was then compared to the temperature of the outer rim measured by the IR camera. However, since the emissivity was used consistently, the resistance to thermal fracture of components relative to each other is still correct. It is only the absolute magnitude of the temperatures that might not be.

This work investigates the effect on thermal fracture resistance of a few design parameters only. Previously, the influence of component size on thermal endurance has been investigated in [16], where smaller components were seen to endure higher temperature than larger ones. The effect of other design parameters, such as, but not limited to, the size of the cavity, the thickness of its top and bottom layers, and the effect of double-sided compared to single-sided heating of components should also be investigated. Since the ultimate goal of heating a thruster is to increase thruster efficiency, the effect of the design parameters on thruster performance, in terms of, e.g. heat transfer to the gas flow, specific impulse and power consumption, also requires further investigation.

In dry testing, the microthrusters reached higher temperatures than the generic components, even though the embedded platinum layers had to be excluded from the thrusters. However, due to the platinum ring at the top and the electrical connector pads at the bottom, there is still a lot of platinum present, possibly serving the function of the embedded platinum layers. Another possible contribution to the increased thermal performance of the thrusters is improved quality from fabrication, most likely in heater quality. This is further supported by the fact that all heaters in the microthrusters were conductive.

The uncertainty in the temperature measurements for the microthrusters is larger than for the generic components. Since large parts of the surface are covered by platinum, only the temperature at a small part of the surface could be assessed during thermal endurance testing of the microthrusters. The temperature distribution is not uniform over the surface. Hence, it is not certain that the area containing

the maximum temperature was assessed. Nevertheless, despite the possible uncertainties, the maximum surface temperature of 1460 °C reached during testing is a great improvement compared to the maximum failure temperature of 679 °C that has been previously reported for dry testing of alumina HTCC microthrusters [16].

A surface temperature of 772 °C during operation is also a great improvement compared to the 307 °C previously reported [16]. However, here it must be noted that the previously investigated thruster was a monopropellant one. Hence, temperatures during operation were attained when it was fed with liquid instead of gas. This affects the thermal performance.

Apart from the high temperatures reached, the rapid heating towards these temperatures should also be noted. To avoid thermal fracture, the temperature has previously been increased very slowly, requiring 25 min to reach the final temperature [16]. In this study, final temperatures during tests of thrusters without tube were reached after 90 s.

The purpose of heating a cold gas thruster is to increase the energy of the gas, which decreases propellant consumption. A measure of how effectively a thruster uses its propellant is the specific impulse, I_{sp}, of the thruster. For a cold gas thruster, $I_{sp} = K\sqrt{T_C/M}$, where T_C is the chamber temperature, M the average molecular weight of the exhaust gases, and K a proportionality constant depending on the specific heats of the exhaust gases and the pressures in the chamber and the ambience [5].

The dimensions of the microthruster are small, and the fixture is designed to keep heat losses to the surroundings as small as possible. Therefore, the temperature differences across the thrusters' vertical axis are most likely small, and the chamber temperature can roughly be estimated as being the same as the measured surface temperature. When operated as a cold gas thruster at constant chamber and ambient pressures, and with a given propellant, increasing the device temperature from the previously observed 307 °C to the maximum operating temperature of 772 °C obtained in this work increases the specific impulse of the thruster with 34%. If the interfacing issues could be mitigated and the maximum temperature of 1460 °C obtained for a stand-alone thruster in this work could be reached during operation, this would cause an increase in specific impulse of 73% compared to operation at 307 °C.

The propellant consumption of a thruster is inversely proportional to its specific impulse [3]. All the propellant that is needed for a space mission needs to be carried on board already at the launch, but electricity on the other hand is abundant as long as the spacecraft is within the reach of the rays from the sun. Hence, heating a cold gas thruster using solar power is a way to make better use of the limited amount of propellant that can be brought.

For current state-of-the art cold gas thrusters, propellant mass is about 15% of total spacecraft mass [6]. In addition, the tanks for compressed gas can add an extra 50% of propellant mass [5]. If less propellant is needed, overall spacecraft mass can be reduced, eventually reducing the cost of a space mission and making missions more generally available. Another option is to use the volume and mass made available from reducing the propellant mass for payload, such as extra instrumentation that can increase the redundancy and success rate of space missions.

5. Conclusions

In this investigation of design parameters' effect on thermal fracture resistance in HTCC microcomponents, peripheral heater location and addition of embedded platinum layers were seen to improve resistance to thermal fracture, whereas choosing circular or square geometries of component and cavity did not affect thermal performance significantly. Choosing a peripheral instead of a central heater location contributed to an increase in failure temperature of 226 °C ± 70 °C, and embedding platinum layers increased the failure temperature with 155 °C ± 70 °C.

Using the optimized design parameters, an alumina microthruster surviving rapid heating from room temperature to 1460 °C was fabricated and evaluated. Furthermore, it could be operated as a cold gas thruster at temperatures up to 772 °C, which is a substantial improvement compared to previously reported device temperatures during operation of 307 °C or lower. This increase in thermal performance can reduce the propellant needed during a space mission, which could either reduce spacecraft mass and costs, or leave room for extra payload with the potential to increase mission success rate.

Data availability statement

The data that support the findings of this study are available upon reasonable request from the authors.

Acknowledgments

The Knut and Alice Wallenberg foundation is acknowledged for funding the laboratory facilities. All contributions from Peter Sturesson at the Ångström Space Technology Centre are highly appreciated.

ORCID iDs

Erika Åkerfeldt https://orcid.org/0000-0003-1215-8633
Lena Klintberg https://orcid.org/0000-0001-7715-3142
Greger Thornell https://orcid.org/0000-0003-4468-6801

References

[1] Rossi C, Do Conto T, Estève D and Larangot B 2001 Design, fabrication and modelling of MEMS-based microthrusters for space application *Smart Mater. Struct.* **10** 1156–62
[2] Markandan K, Chin J K, Cheah K H and Tan M T T 2018 Recent developments in ceramic microthrusters and the potential applications with green propellants: a review *Clean Technol. Environ. Policy* **20** 1941–50
[3] Rossi C 2002 Micropropulsion for space—a survey of MEMS-based micro thrusters and their solid propellant technology *Sens. Update* **10** 257–92

[4] Palmer K, Catalan E V, Lekholm V and Thornell G 2013 Investigation of exhausts from fabricated silicon micronozzles with rectangular and close to rotationally symmetric cross-sections *J. Micromech. Microeng.* **23** 105001
[5] Wertz J R and Larson W J 1999 *Space Mission Analysis and Design* 3rd edn (El Segundo: Microcosm Press and Kluwer Academic Publishers)
[6] Weston S (ed) 2020 *State-of-the-Art Small Spacecraft Technology* (Moffett Field: NASA Ames Reseach Center)
[7] Callister W D and Rethwisch D G 2011 *Materials Science and Engineering: An Introduction* 8th edn (Hoboken: Wiley)
[8] Tan Q, Ren Z, Cai T, Li C, Zheng T, Li S and Xiong J 2015 Wireless passive temperature sensor realized on multilayer HTCC tapes for harsh environment *J. Sens.* **2015** 124058
[9] Lekholm V, Persson A, Klintberg L and Thornell G 2015 Investigation of a zirconia co-fired ceramic calorimetric microsensor for high-temperature flow measurements *J. Micromech. Microeng.* **25** 065014
[10] Sturesson P, Khaji Z, Klintberg L and Thornell G 2017 Ceramic pressure sensor for high temperatures—investigation of the effect of metallization on read range *IEEE Sens. J.* **17** 2411–21
[11] Schubert F, Wollenhaupt S, Kita J, Hagen G and Moos R 2016 Platform to develop exhaust gas sensors manufactured by glass-solder-supported joining of sintered yttria-stabilized zirconia *J. Sens. Sens. Syst.* **5** 25–32
[12] Sturesson P, Khaji Z, Knaust S, Klintberg L and Thornell G 2015 Thermomechanical properties and performance of ceramic resonators for wireless pressure reading at high temperatures *J. Micromech. Microeng.* **25** 095016
[13] Tan Q, Lu F, Ji Y, Wang H, Zhang W and Xiong J 2018 LC temperature–pressure sensor based on HTCC with temperature compensation algorithm for extreme 1100 °C applications *Sens. Actuators* A **280** 437–46
[14] Ritter T, Hagen G, Jaroslaw K, Wiegärtner S, Schubert F and Moos R 2017 Self-heated HTCC-based ceramic disc for mixed potential sensors and for direct conversion sensors for automotive catalysts *Sens. Actuators* B **248** 793–802
[15] Sun W, Cai G, Donadio N, Kuo B, Lee J and Yetter R A 2012 Development of meso-scale co-fired ceramic tape axisymmetric combustors *Int. J. Appl. Ceram Technol.* **9** 833–46
[16] Khaji Z, Klintberg L, Barbade D, Palmer K and Thornell G 2017 Endurance and failure of an alumina-based monopropellant microthruster with integrated heater, catalytic bed and temperature sensors *J. Micromech. Microeng.* **27** 055011
[17] Lekholm V, Persson A, Palmer K, Ericson F and Thornell G 2013 High-temperature zirconia microthruster with an integrated flow sensor *J. Micromech. Microeng.* **23** 055004
[18] Cheah K H and Low K-S 2015 Fabrication and performance evaluation of a high temperature co-fired ceramic vaporizing liquid microthruster *J. Micromech. Microeng.* **25** 015013
[19] Mee R W 2009 *A Comprehensive Guide to Factorial Two-level Experimentation* (New York: Springer)
[20] Khaji Z, Klintberg L and Thornell G 2016 Manufacturing and characterization of a ceramic single-use microvalve *J. Micromech. Microeng.* **26** 095002
[21] Khaji Z, Sturesson P, Klintberg L, Hjort K and Thornell G 2015 Manufacturing and characterization of a ceramic microcombustor with integrated oxygen storage and release element *J. Micromech. Microeng.* **25** 104006
[22] Gongora-Rubio M R, Espinoca-Vallejos P, Sola-Laguna L and Santiago-Avilés J J 2001 Overview of low temperature co-fired ceramics tape technology for meso-system technology (MsST) *Sens. Actuator* A **89** 222–41
[23] Imanaka Y 2005 *Multilayered Low Temperature Cofired Ceramics (LTCC) Technology* (New York: Springer)
[24] Sturesson P, Seton R, Klintberg L, Thornell G and Persson A 2019 Effect of resistive and plasma heating on the specific impulse of a ceramic cold gas thruster *J. Microelectromech. Syst.* **28** 235–44
[25] La Torre F 2011 Gas flow in miniaturized nozzles for micro-thrusters PhD Thesis TU Delft, Delft
[26] Auerkari P 1996 *Mechanical and Physical Properties of Engineering Alumina Ceramics* (Espoo: Technical Research Centre of Finland)
[27] Li W, Feingold A, Palanisamy P and Lorenz G 2012 Co-sintering zirconia electrolyte and insulator tapes for sensor applications *J. Am. Ceram. Soc.* **95** 3815–20
[28] He M Y, Evans A G and Hurchinson J W 1994 Crack deflection at an interface between dissimilar elastic materials: role of residual stresses *Int. J. Solids Struct.* **31** 3443–55
[29] Eriksson L, Johansson E, Kettaneh-Wold N, Trygg J, Wikström C and Wold S 2006 *Multi- and Mega-variate Data Analysis. Part 1: Basic Principles and Applications* 2nd edn (Umeå: Umetrics)